

Article

Multifunctional Electrochemical Properties of Synthesized Non-Precious Iron Oxide Nanostructures

Ruby Phul ¹, M. A. Majeed Khan ², Meryam Sardar ³, Jahangeer Ahmed ^{4,5,*}
and Tokeer Ahmad ^{1,*}

¹ Nanochemistry Laboratory, Department of Chemistry, Jamia Millia Islamia, New Delhi 110025, India; rubyphul@gmail.com

² King Abdullah Institute for Nanotechnology, King Saud University, Riyadh 11451, Saudi Arabia; mmkhan@ksu.edu.sa

³ Enzyme Technology Laboratory, Department of Biosciences, Jamia Millia Islamia, New Delhi 110025, India; msardar@jmi.ac.in

⁴ Department of Chemistry, College of Science, King Saud University, Riyadh 11451, Saudi Arabia

⁵ School of Science and Technology, Glocal University, Saharanapur UP-247001, India

* Correspondence: jahmed@ksu.edu.sa (J.A.); tahmad3@jmi.ac.in (T.A.);

Tel.: +91-11-26981717 (ext. 3261) (T.A.); Fax: +91-11-26980229 (T.A.)

Received: 17 July 2020; Accepted: 25 August 2020; Published: 26 August 2020



Abstract: Magnetic Fe₃O₄ nanostructures for electrochemical water splitting and supercapacitor applications were synthesized by low temperature simple wet-chemical route. The crystal structure and morphology of as-acquired nanostructures were examined by powder X-ray diffraction and transmission electron microscopy. Magnetic measurements indicate that the as-synthesized Fe₃O₄ nanostructures are ferromagnetic at room temperature. The synthesized nanostructures have a high-specific surface area of 268 m²/g, which affects the electrocatalytic activity of the electrode materials. The purity of the as-synthesized nanostructures was affirmed by Raman and X-ray Photoelectron studies. The electrochemical activity of the magnetic iron oxide nanoparticles (MIONPs) for the hydrogen evolution reaction (HER) and supercapacitors were investigated in alkaline medium (0.5 M KOH) versus Ag/AgCl at room temperature. The electrocatalysts show low onset potential (~0.18 V) and Tafel slope (~440 mV/dec) for HER. Additionally, the specific capacitance of MIONPs was investigated, which is to be ~135 ± 5 F/g at 5 mV/s in 1 M KOH.

Keywords: nanostructures; surface area; electrocatalysis; hydrogen evolution; supercapacitor

1. Introduction

Water splitting or electrolysis of water is receiving much attention from researchers due to the diminution of fossil fuels and the increased environmental hazards on account of generating various type of by-products such as dust, smoke, soot, CO₂, etc. [1]. The generation of CO₂ affects the world in the form of global warming, which strikes our lives through rising sea levels due to polar ice cap melt, desertification, and reduced agricultural yields [2,3]. It is necessary to lookup for ample, everlasting, eco-friendly, CO₂-free, and sustainable alternative energy sources [4,5]. Several alternative sources of fuels have already been proposed such as biodiesel, methanol, ethanol, hydrogen, boron, natural gas, liquefied petroleum gas (LPG), electricity, solar fuels, etc. One of these alternative fuels, hydrogen has been believed as a perfect alternative source of fuel, since it has high specific energy, is carbon-neutral, and is the most abundant element in the universe [6,7]. Today 90% of all the H₂ gas has been produced by hydrocarbon reforming, in which hydrocarbons are catalytically oxidized on metal surfaces (Pt, Pd, etc.) at elevated temperatures and results into a mixture of carbon monoxide, carbon dioxide, and hydrogen gas [8,9].

In the present study, we have described electrochemical water splitting to produce H₂ using nanoparticles. Magnetite nanoparticles (Fe₃O₄) attract much attention as they can be used in magnetic storage [10], targeted drug delivery [11], hyperthermia treatments [12], Magnetic resonance imaging (MRI) contrast agents [13], and energy storage systems [14] etc. Supercapacitors are the most promising candidates for electrical storage systems since they have a long cycle life (>100,000 cycles), high power density, simple principle, and fast charge/discharge rate. There are two categories of supercapacitors: electric double-layer capacitors (EDLCs) viz. graphene [15], activated carbon [16], carbon nanotubes [17], etc., as electrode materials and pseudocapacitors such as conducting polymers and metal oxides [18–20]. The electrostatic charge accumulation at the electrode-electrolyte interface is responsible for charge storage in EDLCs, whereas the redox reaction in the electrode is accountable for charge storage in pseudocapacitors. The Fe₃O₄ is considered as electrode material for pseudocapacitors, on account of its natural abundance, low toxicity, low cost, high theoretical specific capacity (2299 F/g) [21], large potential window (−1.2 to 0.25 V), high conductivity ($\sigma = 2 \times 10^4 \text{ Sm}^{-1}$), etc. Since iron oxide nanoparticles could be easily separated from the reaction media by a simple magnetic separation; therefore, it can be used as a promising material for catalytic reactions.

Transition metal oxides have garnered attention for water splitting due to their fascinating electrocatalytic activity, low-cost, low toxicity, and earth abundance. They show excellent oxygen evolution reaction (OER) potential, but due to low hydrogen desorption ability, their HER reactivity is poor [22,23]. Transition metal oxides have good oxygen evolution reaction (OER) and oxygen reduction reaction (ORR) performance within single material in a synergistic effect owing to the ability to mix. Currently, scientists are working to develop efficient metal oxide-based catalysts for HER with high stability, low-toxicity, and fast reaction kinetics with desirable efficiencies. The efficiency of the catalytic materials could be tuned by combining them with other materials such as graphene, carbon nanotubes, organometallic frameworks, etc. In 1977, Nakamura [24] used iron oxide for thermochemical water splitting. Afterward, scientists have studied several metal oxide materials for water splitting [25–29]. At present, there is no report regarding the electrochemical water splitting for HER using MIONPs.

Numerous chemical methods have been reported in the literature for the synthesis of various metal-oxide nanoparticles such as reverse micelle [30,31], hydrothermal [32], solvothermal [33,34], sol-gel [35], co-precipitation [36], and polymeric precursor [37–39] methods. Luo et al. synthesized core-shell nano-heterostructures of Fe₃O₄@NiFe_xO_y at low temperature, which showed utmost electrocatalytic performance for OER in carbonate electrolyte [40]. Zhang et al. constructed the phosphorus-doped inverse spinel Fe₃O₄ electrocatalyst on iron foam (P-Fe₃O₄/IF) for alkaline H₂ production. The synthesized electrocatalyst showed noteworthy performance at a very low overpotential of 1.38 V at 100 mA/cm² [41]. Further, phosphorus-doped Fe₃O₄ nanoflowers were developed on a 3D graphene (P-Fe₃O₄@3DG) substrate using hydrothermal and low-temperature phosphating reaction. The P-Fe₃O₄@3DG composite possessed exceptional performance for HER at a low overpotential of 1.23 V at 10 mA/cm², prominent stability up to 50 h and Tafel slope value of 65 mV/dec. The synthesized electrocatalyst exhibited excellent performance in a wide range of pH [42]. Herein, we report the wet-chemical synthesis of magnetic Fe₃O₄ nanoparticles for clean energy. The three-electrode electrochemical work station has been used to investigate the catalytic performance of MIONPs for HER. Additionally, the supercapacitive behavior of MIONPs has also been studied. The as-synthesized nanoparticles were successfully investigated by powder X-ray diffraction (PXRD), high-resolution transmission electron microscopy (HRTEM), BET surface area analysis, magnetization study, Raman, and X-ray photoelectron spectroscopy.

2. Materials and Methods

2.1. Synthesis of Magnetic Iron Oxide Nanoparticles

Iron (II) sulfate heptahydrate was purchased from Fisher Scientific, (98% purity), sodium hydroxide pellets, and sodium nitrate were bought from Merck Ltd. (99% purity). All the chemicals were used as received without further purification.

Magnetic iron oxide nanoparticles (MIONPs) were synthesized by a simple wet-chemical route as per the literature [43]. In a typical procedure, 3 mmol of Fe^{2+} salt was dissolved in 120 mL distilled water, and the solution was stirred till the temperature of 80 °C was reached. Now, 30 mmol of NaOH and 3 mmol of NaNO_3 were dissolved in 30 mL of distilled water and added dropwise to the above solution with constant stirring. The mixture was refluxed for 2 h at 80 °C forming black precipitates. The precipitates were collected by a permanent magnet and washed several times with double distilled water till the pH~7. The black precipitates were dried at 100 °C in an open-air oven for 12 h to obtain the pure Fe_3O_4 phase of MIONPs.

2.2. Physical Characterization

Rigaku Ultima IV X-ray diffractometer with Ni-filtered $\text{Cu-K}\alpha$ radiation ($\lambda = 1.5416 \text{ \AA}$) was used to determine the crystalline structure of MIONPs. The diffraction pattern was collected at a step size of 0.05° and a step time of 1 s and 2θ range from 20° to 70° . Transmission electron microscopic (TEM) analysis was carried out on an FEI Technai G^2 20 HRTEM with an accelerating voltage of 200 kV. TEM samples were prepared by putting a drop of dispersed sample on a carbon-coated copper grid and dried in air for 1 h. The surface area and the pore size of as-synthesized iron oxide nanoparticles were determined using BET surface area analyzer (Model: Nova 2000e, Quantachrome Instruments Limited, USA) at liquid nitrogen temperature (77 K). Before analysis, the samples were degassed at 150 °C for 3 h in a vacuum degassing mode to remove the surface contaminants such as water vapor and adsorbed gases. The specific surface area was calculated using the multipoint BET equation. The pore size distributions were determined from the N_2 desorption isotherms at 77 K using the Dubinin–Astakhov (DA) method. The Raman spectrum was recorded on a Renishaw Raman spectrometer with an Ar-laser source (488 nm) at ambient conditions. The X-ray photoelectron spectroscopy (XPS) scans were carried out to confirm the oxidation state of the MIONPs using Kratos-Axis-Ultra DLD (Chestnut Ridge, NY, USA) spectrometer with Al $\text{K}\alpha$ X-ray source. The magnetization study has been performed using a magnetic property measurement system Vibrating Sample Magnetometer (VSM 7300, Lakeshore, Carson, CA, USA) under an external magnetic field of $\pm 120 \text{ kOe}$ at 300 K.

2.3. Electrochemical Measurements

The cyclic voltammetry (CV), linear sweep voltammetry (LSV), chrono-amperometry (CA), and Tafel studies were carried out with a three electrode electrochemical work station (potentiostat/galvanostat, CHI 660E, China) at room temperature in alkaline medium (0.5 M KOH) to investigate the redox behavior of the as-synthesized nanoparticles via electrolysis of water. Pt wire was used as a counter electrode, Ag/AgCl as the reference electrode, and glassy carbon as the working electrode. The working electrodes were prepared by putting a drop of slurry (containing 2.5 mg of catalysts to 0.5 mL of isopropanol with 0.1 mL of Nafion solution followed by the sonication for 10 min) onto the glassy carbon and then dried at 60 °C in a vacuum oven [44]. The loaded amount of the nanoparticles was of $\sim 0.24 \text{ mg/cm}^2$ on the GC electrode, and the area of the working electrode was 0.07 cm^2 . Freshly prepared electrodes were used for the electrochemical measurements. The CV of the iron oxide nanoparticles for HER was investigated in a peak window from 0 to -1.4 V versus Ag/AgCl at the various scan rates (i.e., 25, 50, 100 mV/s). The LSV and Tafel measurements for electrolysis of water were also carried out at 25 mV/s and 10 mV/s, respectively, in 0.5 M KOH vs. Ag/AgCl. The stability and activity of the iron oxide electrodes were also tested by CA measurements for HER at the fixed potential (i.e., -1.4 V vs. Ag/AgCl) for 20 s in 0.5 M KOH. The supercapacitive performance

was also investigated in the potential window from -0.3 to $+0.5$ V at the scan rate of $5\text{--}100$ mV/s in 1 M KOH. The electrode for specific capacitance study was prepared by pasting the slurry (MIONPs: Carbon black: PVDF of $75:15:10$) onto the surface of nickel foam (1 cm²). The loaded amount of the sample was 1 mg. Charge-discharge (CD) studies of MIONPs were carried out in the potential window of 550 mV for 50 segments.

3. Results and Discussion

3.1. X-ray Diffraction Studies

Powder X-ray diffraction pattern of as-synthesized nanoparticles confirmed the presence of the magnetite phase (Figure 1). The diffraction peaks indexed as planes (220), (311), (222), (400), (331), (422), (333), and (440) correspond to a cubic unit cell with lattice parameter $a = 8.394$, the most potent reflection at the (311) plane is also the characteristic of cubic phase which confirms that the structure obtained for magnetite nanoparticles is an inverse spinel-type oxide (Space group: $Fd\bar{3}m$) [45]. All the peaks could be indexed in pure cubic phase Fe_3O_4 and are in good agreement with standard magnetite, JCPDS No. 079-0417.

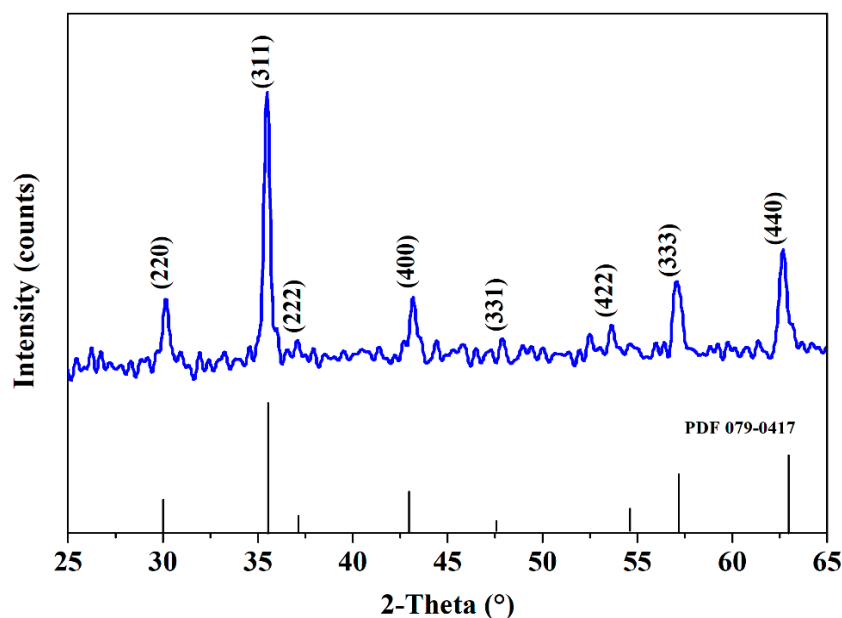


Figure 1. Powder X-Ray diffraction pattern of MIONPs.

3.2. Electron Microscopic Studies

The morphological study was carried out by transmission electron microscopy (TEM) to recognize the size and morphology of MIONPs. The TEM image of MIONPs reveals that the nanoparticles are monodispersed and cube-shaped, as also shown in Figure 2a. The average particle size was calculated using ImageJ software and found to be 42 nm. Furthermore, high-resolution transmission electron microscopy (HRTEM) analysis was done to interpret the crystallinity, phase, and growth direction of as-synthesized MIONPs. Figure 2b shows a typical HRTEM image of MIONPs which visualizes well-resolved lattice fringes with an average lattice distance of 2.489 ± 0.04 Å, which corresponds to the most intense peak (311) of MIONPs. The selected area electron diffraction (SAED) pattern of MIONPs (Figure 2c) shows sharp diffraction spots, indicating the well-developed nanocrystalline structure. The different lattice planes of MIONPs (440), (422), (311), and (220) were assigned to the diffraction rings in the SAED pattern, which are in accordance with the XRD pattern.

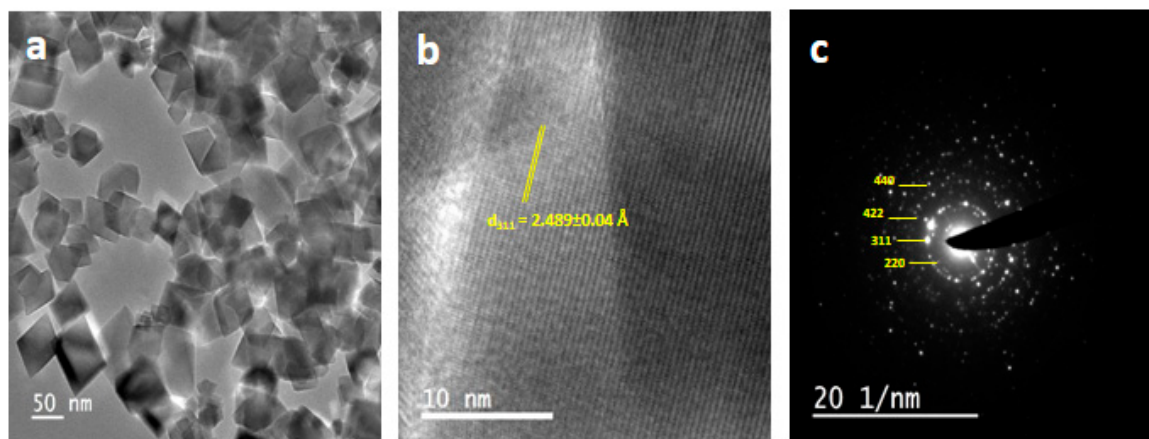


Figure 2. (a) TEM micrograph, (b) HR-TEM image and (c) SAED pattern of MIONPs.

3.3. Magnetic Properties

The vibrating sample magnetometer (VSM) was used to investigate the magnetic behavior of Fe_3O_4 nanoparticles at room temperature between -10 to 10 kOe. Figure 3 clearly showed the ferromagnetic nature of the as-synthesized nanoparticles. The saturation magnetization (M_s), remanent magnetization (M_r), and coercivity (H_c) of MIONPs were 68 emu/g, 13.90 emu/g, and 100 Oe, respectively. The saturation magnetization (M_s) value for MIONPs was lower than the M_s value of the corresponding bulk Fe_3O_4 (92 emu/g) [46]. The difference might be attributed to a smaller size, larger surface area/volume ratio, and spin canting effects at the surface [47].

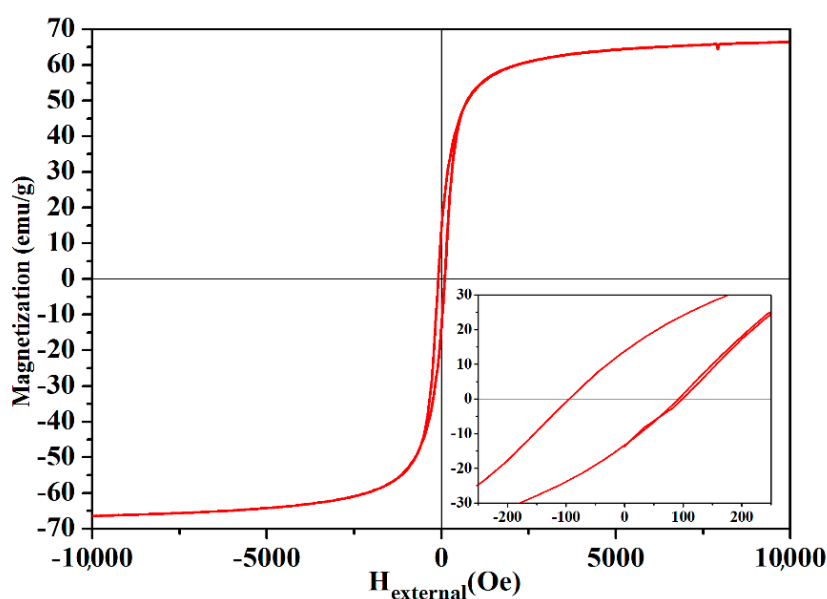


Figure 3. The magnetization curve (M-H) measured at room temperature for MIONPs; the inset shows a magnified view of the hysteresis loop.

3.4. BET Surface Area Studies

The multipoint BET method was used to determine the specific surface area of as-prepared MIONPs. Figure 4a represents the nitrogen adsorption-desorption isotherm for MIONPs. The isotherm indicates that the as-synthesized nanoparticles have a porosity of type IV, which is associated with capillary condensation in mesoporous, and the isotherm shows a distinct hysteresis loop in the range of 0.7 – 1.0 P/P_0 [48]. The specific surface area of as-synthesized nanoparticles was found to be 268 m^2/g ,

which is comparatively higher than earlier reports [49,50]. Figure 4b shows the DA plot, which gives a pore radius of 14.8 Å for MIONPs.

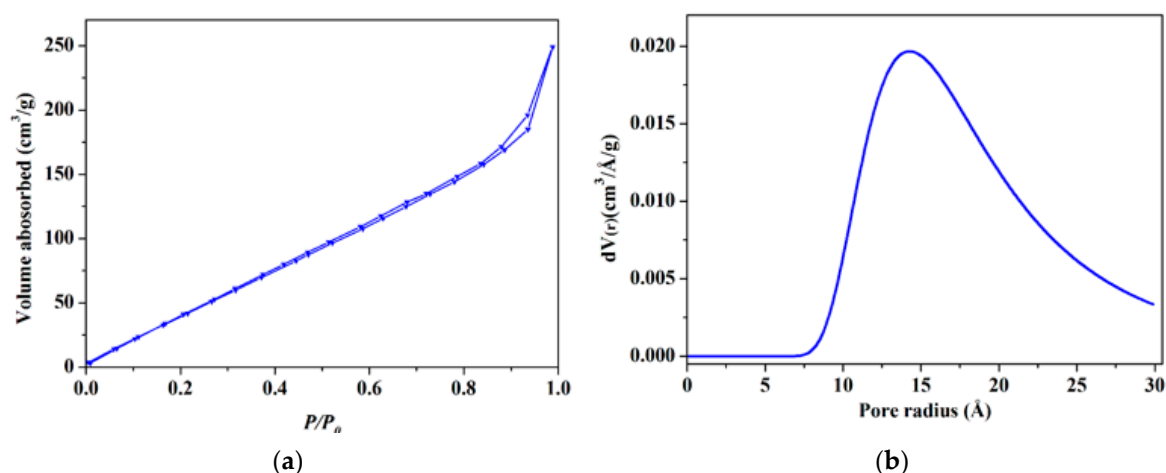


Figure 4. (a) Nitrogen adsorption/desorption isotherm and (b) DA pore size distribution plot of MIONPs.

3.5. Raman Studies

Figure 5 represents the Raman spectrum of MIONPs recorded in the wavelength range of 200–1000 cm^{-1} . The spectrum shows a sharp peak at 670 cm^{-1} , corresponding to A1g mode, depicting a symmetric stretch of oxygen atoms along with Fe–O bonds [51]. The peaks at ~515 and 535 cm^{-1} could be attributed to Eg and T2g modes, respectively. The T2g mode ascribes the asymmetric stretch of Fe and O atoms [52,53]. The Raman spectra confirm the absence of any other form of iron oxide, i.e., hematite or maghemite, indicating the purity of the as-synthesized nanoparticles [54].

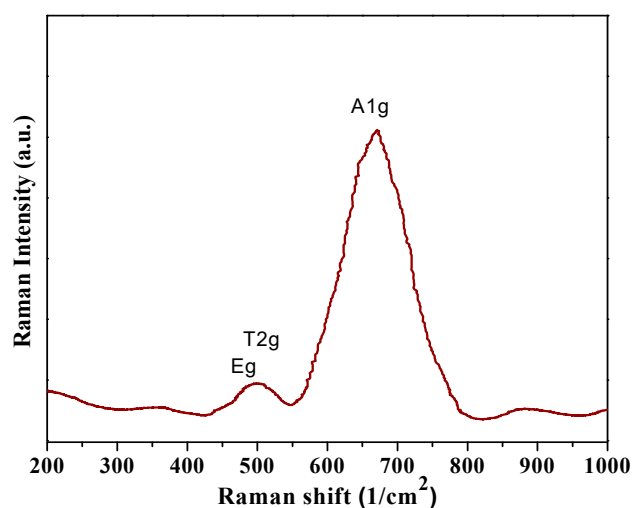


Figure 5. The Raman spectrum recorded at room temperature for MIONPs.

3.6. X-ray Photoelectron Spectroscopic Studies

The X-ray photoelectron spectroscopic study was carried out to determine the electronic structure and chemical composition of MIONPs. The full XPS spectrum shown in Figure 6a reveals the presence of oxygen and iron of MIONPs. The high-resolution Fe 2p spectrum (Figure 6b) shows two spin-orbit peaks at 711.3, and 723.5 eV corresponding to binding energies of Fe 2p_{3/2} and Fe 2p_{1/2} peaks of Fe₃O₄, respectively [53,54]. The peaks are broad due to the presence of both Fe²⁺ and Fe³⁺ ions, as Fe₃O₄ is the blend of FeO and Fe₂O₃. Further, the non-occurrence of satellite peaks at around 718 eV, which is the unique feature of the electronic structure of Fe₂O₃ [55], affirms the presence of pure Fe₃O₄. The other

peaks around 708.3 and 723 eV (Fe^{2+}) and 712.8 eV (Fe^{3+}) could be assigned to the Fe–O bond [55]. Figure 6c shows the high-resolution O 1s spectrum with a strong peak at 531 eV, representing the Fe–O bonds. The Fe 2p and O 1s spectra are in good agreement with the standard Fe_3O_4 spectrum, hence confirming that the as-synthesized nanoparticles were pure Fe_3O_4 .

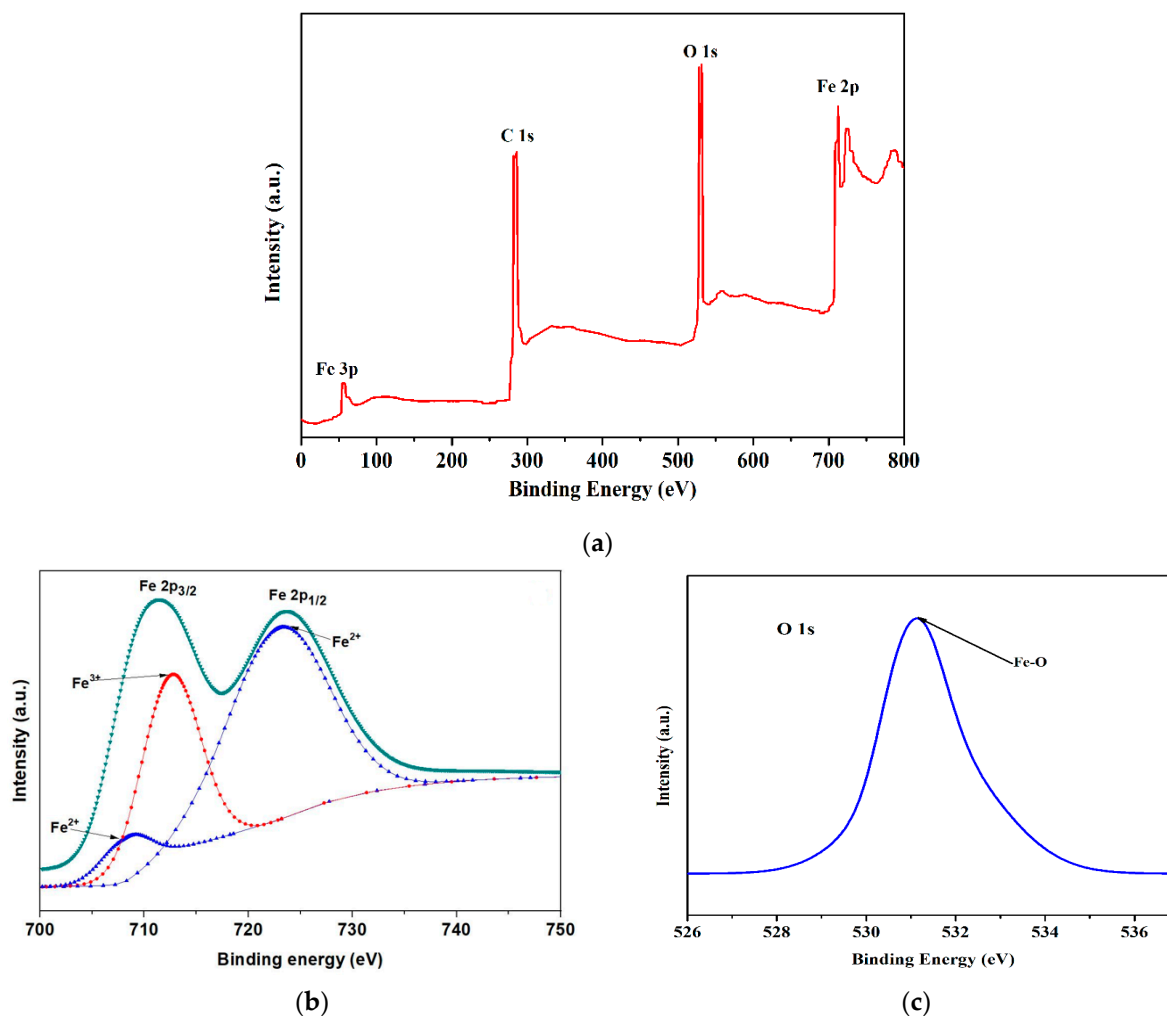


Figure 6. (a) Full XPS spectrum, (b) High-resolution XPS spectrum of Fe 2p and (c) High-resolution XPS spectrum of O 1s of MIONPs.

3.7. Electrocatalytic Studies

The electrocatalytic activity of as-synthesized MIONPs for HER and super-capacitive performances were conducted in 0.5 M KOH electrolyte solution. The cyclic voltammograms of MIONPs at the various scan rates (i.e., 25, 50, 100 mV/s) are depicted in Figure 7a. The redox behavior of MIONPs was observed in the applied potential window, with a redox peak at -0.65 V vs. Ag/AgCl (~ 1.25 V vs. RHE) ascribed to the redox reaction of iron (i.e., $\text{Fe}^{2+}/\text{Fe}^{3+}$) as reported elsewhere [56,57]. The LSV measurement was carried out to measure the current for the water-splitting reaction, with an onset potential of -0.62 V vs. Ag/AgCl (0.35 V vs. RHE) for the HER as shown in Figure 7b. The electrochemical analysis affirms that the observed cathodic faradaic steady current was efficient during the cathodic sweep (i.e., HER), while the low anodic faradaic steady current was observed toward the anodic sweep (i.e., OER). This is notable that the resulting current density (current/area of the electrode) of the electrode is directly

related to the amount of H₂ and O₂ evolution from the water electrolysis. The electrochemical reactions for the water splitting reaction at the cathodic/anodic potentials are shown as given:

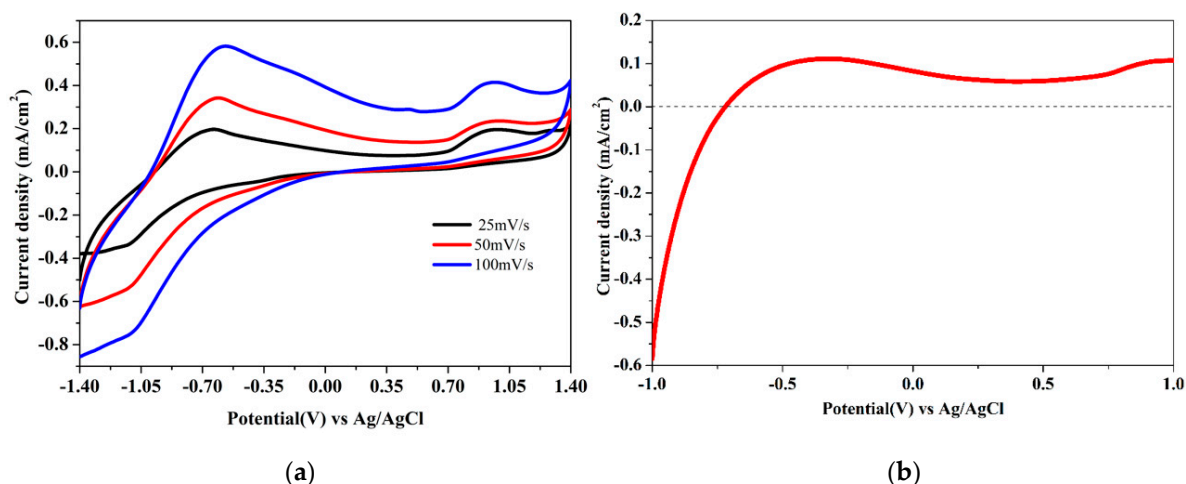
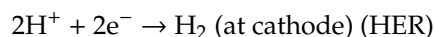
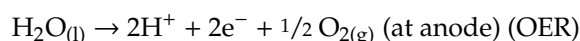


Figure 7. (a) Cyclic voltammograms (CV) of the MIONPs and (b) Linear sweep voltammetry (LSV) obtained for MIONPs in 0.5 M KOH.

The catalytic activity of MIONPs towards HER was analyzed in 0.5 M KOH in the potential range from 0 to -1.4 V vs. Ag/AgCl. Figure 8a,b shows the CV and LSV profile of MIONPs for H₂ generation at a scan rate of 100 mV/s. The linear sweep polarization curve reveals the generation of hydrogen at an overpotential value of ~ 0.75 V vs. Ag/AgCl (~ 0.18 V vs. RHE) is expected to achieve a low current density of 0.45 mA/cm². The current density is directly correlated with the amount of H₂ evolved. The current density of MIONPs was calculated by the current/geometric electroactive surface area of electrode, and the geometric electroactive surface area of the working electrode could be estimated from the Randles–Sevik equation [58]. The resulting current density of MIONPs depends on the size, surface area, morphology, and orientation of electrocatalysts [59,60]. The MIONPs exhibits high surface area with strong dipole interaction within the Fe₃O₄ nanoparticles, which provides enough space to the dissemination of the electrolyte to the active sites of the electrode, enhancing the electrochemical activity. The stability and activity of MIONPs were tested by CA studies at the steady potential of -1.4 V vs. Ag/AgCl for 40 s, as shown in Figure 8c. Chronoamperometric measurements (i.e., the epotentiostatic quantitative measurements) were done to check the stability and electrocatalytic activity of the electrode materials at a fixed potential with time. Note that the electrochemical water-splitting reaction stops and the current drop drastically to zero due to the switched off the potential (Figure 8c). The mechanism of HER activity was demonstrated by the Tafel plot (Figure 8d), which is derived by the polarization curve using the Tafel equation:

$$\eta = b \times \log(J/J_0)$$

where η , b , J , and J_0 corresponds to the over potential, Tafel slope, current density, and exchange current density of the electrocatalytic reaction, respectively. The Tafel slope value of the MIONPs was found to be ~ 440 mV/dec from the linear fitted Tafel polarization curve of MIONPs for HER. Note that the experimental error could be ± 5 . The effective electro-active catalysts for water splitting could lower the Tafel slope values to sustain the high activity and stability to enhance the efficiency due to the loss of low energy during the electrochemical reactions.

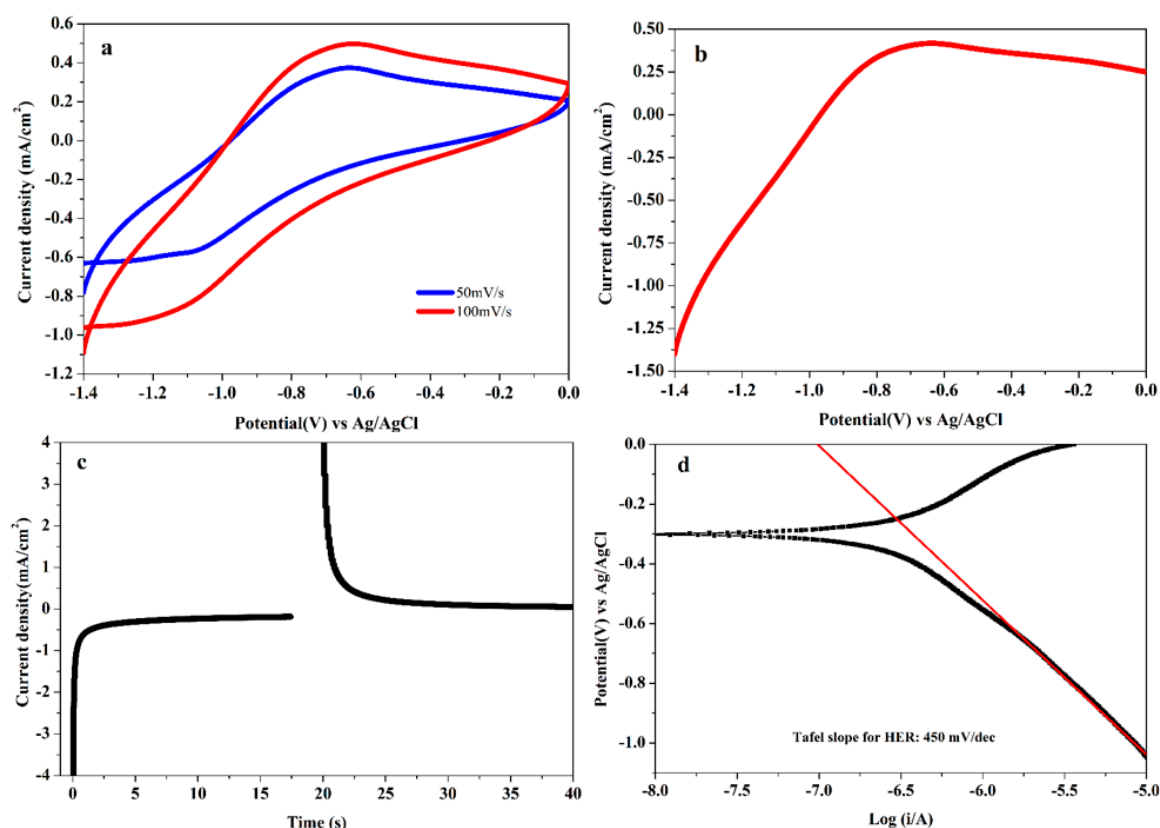


Figure 8. (a) Cyclic voltammograms of MIONPs in 0.5 M KOH by applying the potential range from 0 to -1.4 V vs. Ag/AgCl with a scan rate of 50 mV/s and 100 mV/s; (b) Linear sweep voltammetry for MIONPs at 100 mV/s; (c) Chronoamperometric (CA) studies of MIONPs on glassy carbon electrode at -1.4 V; and (d) Tafel plot at 10 mV/s for H_2 generation.

Further, we also investigated the supercapacitive behavior of MIONPs at 5 mV/s scan rate in 1 M KOH with a three-electrode system. The CV curves of the MIONPs (Figure 9a) were recorded at a scan rate from 5 to 100 mV/s in the potential window from -0.3 to 0.5 V vs. Ag/AgCl. The area under the CV curves suggests efficient supercapacitive behavior of the electrode material. The change in the current response could be due to the large surface area of nanoparticles [61]. A hysteresis under the broad potential range reveals that the as-prepared material could be useful in energy storage applications. The specific capacitance of MIONPs at 5 mV/s was calculated using the following equations:

$$C_s = (\int I(V)dv)/(vm\Delta V)$$

The term symbols of the above equation could be identified as C_s , $\int I(V)dv$, v , m , and ΔV of the specific capacitance, an integrated area under the CV curve, scan rate, mass of the catalysts, and voltage window, respectively. Figure 9b shows the specific capacitance of MIONPs from CV tests with different scan rates, and the high specific capacitance is found to be $\sim 135 \pm 5$ F/g at the scan rate of 5 mV/s. The stability/durability of the MIONPs was checked by galvanostatic charge-discharge (GCD) measurements at 1×10^{-5} A in a potential window of 550 mV for 50 segments, and it was observed that the electrode material shows excellent cycling stability with consistent specific capacitance, i.e., $\sim 95\%$ of the specific capacitance is retained (Figure 9c). The supercapacitive performance of MIONPs could be due to good electrical conductivity and the high surface area of the material. A comparison of the specific capacitance of the material under consideration (MIONPs) with the reported literature has been tabulated in Table 1.

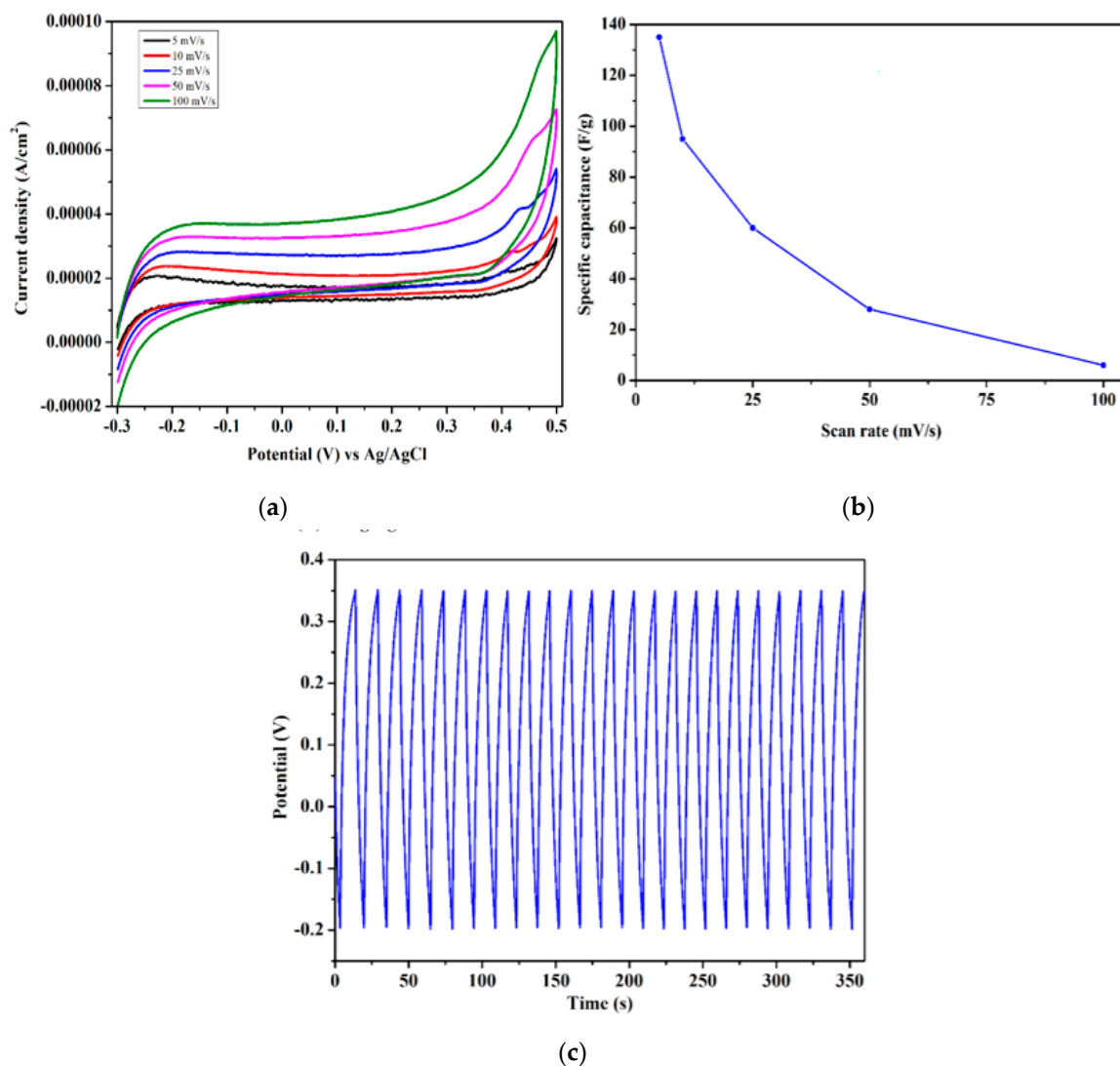


Figure 9. (a) Cyclic voltammograms at 5 to 100 mV/s scan rates, (b) Specific capacitances of the MIONPs electrode as a function of scan rate and (c) charge/discharge profile of MIONPs.

Table 1. Comparison of specific capacitances with electrochemical parameters of as-acquired MIONPs with the literature.

Catalyst	Electrolyte	Method	Scan Rate (mV/s)	Cs (F/g)	Ref.
Fe ₃ O ₄	3 M KOH	Sol-Gel	20	185	[19]
(AC)-Fe ₃ O ₄	6 M KOH	Microwave	10	37.9	[62]
CNT/Fe ₃ O ₄	6 M KOH	Hydrothermal	10	117.2	[63]
Pyrrole treated Fe ₃ O ₄ film	0.1 M Na ₂ SO ₃	Hydrothermal/spray deposition	10	190	[64]
CoFe ₂ O ₄	5.0 M KOH	Polymeric Route	5	94	[65]
Porous Fe ₃ O ₄ /carbon composite	1 M KOH	Calcination	50	139	[66]
Fe ₃ O ₄	0.5 M KOH	Co-precipitation	5	135	Present

4. Conclusions

In summary, we have thrived, easily recoverable magnetic iron oxide nanostructures at low temperatures via a simple co-precipitation method. These magnetic nanoparticles have an inverse

spinel structure, which was confirmed by PXRD. The used precursors can distinctly evolve the cubic shaped nanoparticles having a size ~42 nm. The magnetic studies confirmed the ferromagnetic nature of nanoparticles. The current report successfully demonstrated the ability of magnetic iron oxide nanoparticles for electrochemical water splitting and supercapacitor applications. The large surface area of nanoparticles, as confirmed by BET, provides the surface for water-splitting reactions. This contribution can be important for developing a versatile synthetic pathway for easily recoverable magnetic nanoparticles as well as clean energy and storage.

Author Contributions: Conceptualization, T.A.; Data curation, J.A.; Formal analysis, R.P. and M.S.; Funding acquisition, M.A.M.K.; Investigation, T.A.; Methodology, R.P.; Resources, M.A.M.K., J.A. and T.A.; Writing—original draft, R.P. and T.A.; Writing—review & editing, J.A. and T.A. All authors have read and agreed to the published version of the manuscript.

Funding: This research was funded by the MHRD-SPARC scheme of Govt. of India, grant number: SPARC/2018-2019/P843/SL and King Saud University, Riyadh, Saudi Arabia, grant number: RSP-2020/130.

Acknowledgments: T.A. thanks for Govt. of India for financial support. R.P. specially thanks to UGC, New Delhi, for the Senior Research Fellowship. The authors also acknowledge the measurement support provided through the DST PURSE program at CIF, Jamia Millia Islamia, and thank JNCASR, Bengaluru, for the electron microscopic and VSM studies. The authors extend their sincere appreciation to King Saud University, Riyadh, Saudi Arabia, for funding this research.

Conflicts of Interest: The authors declare no conflict of interest.

References

1. Habas, S.E.; Platt, H.A.S.; van Hest, M.F.A.M.; Ginley, D.S. Low-Cost Inorganic Solar Cells: From Ink To Printed Device. *Chem. Rev.* **2010**, *110*, 6571–6594. [[CrossRef](#)]
2. Lewis, N.S.; Nocera, D.G. Powering the planet: Chemical challenges in solar energy utilization. *Proc. Natl. Acad. Sci. USA* **2006**, *103*, 15729–15735. [[CrossRef](#)]
3. Solomon, S.; Plattner, G.-K.; Knutti, R.; Friedlingstein, P. Irreversible climate change due to carbon dioxide emissions. *Proc. Natl. Acad. Sci. USA* **2009**, *106*, 1704–1709. [[CrossRef](#)] [[PubMed](#)]
4. Bard, A.J.; Fox, M.A. Artificial Photosynthesis: Solar Splitting of Water to Hydrogen and Oxygen. *Acc. Chem. Res.* **1995**, *28*, 141–145. [[CrossRef](#)]
5. Chow, J.; Kopp, R.J.; Portney, P.R. Energy Resources and Global Development. *Science* **2003**, *302*, 1528–1531. [[CrossRef](#)] [[PubMed](#)]
6. Balat, M. Potential importance of hydrogen as a future solution to environmental and transportation problems. *Int. J. Hydrog. Energy* **2008**, *33*, 4013–4029. [[CrossRef](#)]
7. Campen, A.; Mondal, K.; Wiltowski, T. Separation of hydrogen from syngas using a regenerative system. *Int. J. Hydrog. Energy* **2008**, *33*, 332–339. [[CrossRef](#)]
8. Muradov, N.Z.; Veziroğlu, T.N. From hydrocarbon to hydrogen-carbon to hydrogen economy. *Int. J. Hydrog. Energy* **2005**, *30*, 225–237. [[CrossRef](#)]
9. Haryanto, A.; Fernando, S.; Murali, N.; Adhikari, S. Current Status of Hydrogen Production Techniques by Steam Reforming of Ethanol: A Review. *Energy Fuels* **2005**, *19*, 2098–2106. [[CrossRef](#)]
10. Fried, T.; Shemer, G.; Markovich, G. Ordered Two-Dimensional Arrays of Ferrite Nanoparticles. *Adv. Mater.* **2001**, *13*, 1158–1161. [[CrossRef](#)]
11. Kim, J.; Lee, J.E.; Lee, S.H.; Yu, J.H.; Lee, J.H.; Park, T.G.; Hyeon, T. Designed Fabrication of a Multifunctional Polymer Nanomedical Platform for Simultaneous Cancer-Targeted Imaging and Magnetically Guided Drug Delivery. *Adv. Mater.* **2008**, *20*, 478–483. [[CrossRef](#)]
12. Lee, H.; Yu, M.K.; Park, S.; Moon, S.; Min, J.J.; Jeong, Y.Y.; Kang, H.-W.; Jon, S. Thermally Cross-Linked Superparamagnetic Iron Oxide Nanoparticles: Synthesis and Application as a Dual Imaging Probe for Cancer in Vivo. *J. Am. Chem. Soc.* **2007**, *129*, 12739–12745. [[CrossRef](#)] [[PubMed](#)]
13. Ahmad, T.; Phul, R. Magnetic Iron Oxide Nanoparticles as Contrast Agents: Hydrothermal Synthesis, Characterization and Properties. *Solid State Phenom.* **2015**, *232*, 111–145. [[CrossRef](#)]
14. Nithya, V.D.; Sabari Arul, N. Progress and development of Fe₃O₄ electrodes for supercapacitors. *J. Mater. Chem. A* **2016**, *4*, 10767–10778. [[CrossRef](#)]

15. Zhang, X.; Zhang, H.; Li, C.; Wang, K.; Sun, X.; Ma, Y. Recent advances in porous graphene materials for supercapacitor applications. *RSC Adv.* **2014**, *4*, 45862–45884. [[CrossRef](#)]
16. Divyashree, A.; Hegde, G. Activated carbon nanospheres derived from bio-waste materials for supercapacitor applications—A review. *RSC Adv.* **2015**, *5*, 88339–88352. [[CrossRef](#)]
17. Pan, H.; Li, J.; Feng, Y. Carbon Nanotubes for Supercapacitor. *Nanoscale Res. Lett.* **2010**, *5*, 654. [[CrossRef](#)]
18. Wang, C.; Xu, J.; Yuen, M.-F.; Zhang, J.; Li, Y.; Chen, X.; Zhang, W. Hierarchical Composite Electrodes of Nickel Oxide Nanoflake 3D Graphene for High-Performance Pseudocapacitors. *Adv. Funct. Mater.* **2014**, *24*, 6372–6380. [[CrossRef](#)]
19. Mitchell, E.; Gupta, R.K.; Mensah-Darkwa, K.; Kumar, D.; Ramasamy, K.; Gupta, B.K.; Kahol, P. Facile synthesis and morphogenesis of superparamagnetic iron oxide nanoparticles for high-performance supercapacitor applications. *New J. Chem.* **2014**, *38*, 4344–4350. [[CrossRef](#)]
20. Chaudhari, N.K.; Chaudhari, S.; Yu, J.-S. Cube-like α -Fe₂O₃ Supported on Ordered Multimodal Porous Carbon as High Performance Electrode Material for Supercapacitors. *ChemSusChem* **2014**, *7*, 3102–3111. [[CrossRef](#)] [[PubMed](#)]
21. Chen, X.; Chen, K.; Wang, H.; Xue, D. Composition Design upon Iron Element toward Supercapacitor Electrode Materials. *Mater. Focus* **2015**, *4*, 78–80. [[CrossRef](#)]
22. Zhang, T.; Wu, M.-Y.; Yan, D.-Y.; Mao, J.; Liu, H.; Hu, W.-B.; Du, X.-W.; Ling, T.; Qiao, S.-Z. Engineering oxygen vacancy on NiO nanorod arrays for alkaline hydrogen evolution. *Nano Energy* **2018**, *43*, 103–109. [[CrossRef](#)]
23. Yang, L.; Zhou, H.; Qin, X.; Guo, X.; Cui, G.; Asiri, A.M.; Sun, X. Cathodic electrochemical activation of Co₃O₄ nanoarrays: A smart strategy to significantly boost the hydrogen evolution activity. *Chem. Commun.* **2018**, *54*, 2150–2153. [[CrossRef](#)] [[PubMed](#)]
24. Nakamura, T. Hydrogen production from water utilizing solar heat at high temperatures. *Sol. Energy* **1977**, *19*, 467–475. [[CrossRef](#)]
25. Scheffe, J.R.; Li, J.; Weimer, A.W. A spinel ferrite/hercynite water-splitting redox cycle. *Int. J. Hydrog. Energy* **2010**, *35*, 3333–3340. [[CrossRef](#)]
26. Gokon, N.; Kondo, K.; Hatamachi, T.; Sato, M.; Kodama, T. Oxygen-releasing step of nickel ferrite based on Rietveld analysis for thermochemical two-step water-splitting. *Int. J. Hydrog. Energy* **2013**, *38*, 4935–4944. [[CrossRef](#)]
27. Bader, R.; Venstrom, L.J.; Davidson, J.H.; Lipiński, W. Thermodynamic Analysis of Isothermal Redox Cycling of Ceria for Solar Fuel Production. *Energy Fuels* **2013**, *27*, 5533–5544. [[CrossRef](#)]
28. Loutzenhiser, P.G.; Steinfeld, A. Solar syngas production from CO₂ and H₂O in a two-step thermochemical cycle via Zn/ZnO redox reactions: Thermodynamic cycle analysis. *Int. J. Hydrog. Energy* **2011**, *36*, 12141–12147. [[CrossRef](#)]
29. Ahmed, J.; Poltavets, V.V.; Prakash, J.; Alshehri, S.M.; Ahmad, T. Sol-Gel synthesis, structural characterization and bifunctional catalytic activity of nanocrystalline delafossite CuGaO₂ particles. *J. Alloy. Compd.* **2016**, *688*, 1157–1161. [[CrossRef](#)]
30. Ganguli, A.K.; Ahmad, T. Nanorods of Iron Oxalate Synthesized Using Reverse Micelles: Facile Route for α -Fe₂O₃ and Fe₃O₄ Nanoparticles. *J. Nanosci. Nanotechnol.* **2007**, *7*, 2029–2035. [[CrossRef](#)]
31. Ahmad, T.; Ganguli, A.K. Structural and Dielectric Characterization of Nanocrystalline (Ba,Pb)ZrO₃ Developed by Reverse Micellar Synthesis. *J. Am. Ceram. Soc.* **2006**, *89*, 3140–3146. [[CrossRef](#)]
32. Ganguly, A.; Ahmad, T.; Ganguli, A.K. Silica Mesostructures: Control of Pore Size and Surface Area Using a Surfactant-Templated Hydrothermal Process. *Langmuir* **2010**, *26*, 14901–14908. [[CrossRef](#)] [[PubMed](#)]
33. Ahmad, T.; Khatoon, S.; Coolahan, K.; Lofland, S.E. Solvothermal synthesis, optical and magnetic properties of nanocrystalline Cd_{1-x}Mn_xO (0.04 < x = 0.10) solid solutions. *J. Alloy. Compd.* **2013**, *558*, 117–124. [[CrossRef](#)]
34. Khatoon, S.; Coolahan, K.; Lofland, S.E.; Ahmad, T. Optical and magnetic properties of solid solutions of In_{2-x}Mn_xO₃ (0.05, 0.10 and 0.15) nanoparticles. *J. Alloy. Compd.* **2012**, *545*, 162–167. [[CrossRef](#)]
35. Sui, R.; Charpentier, P. Synthesis of Metal Oxide Nanostructures by Direct Sol–Gel Chemistry in Supercritical Fluids. *Chem. Rev.* **2012**, *112*, 3057–3082. [[CrossRef](#)] [[PubMed](#)]
36. Ahmad, T.; Phul, R.; Khatoon, N.; Sardar, M. Antibacterial efficacy of Ocimum sanctum leaf extract-treated iron oxide nanoparticles. *New J. Chem.* **2017**, *41*, 2055–2061. [[CrossRef](#)]

37. Ahmad, T.; Lone, I.H.; Ansari, S.G.; Ahmed, J.; Ahamad, T.; Alshehri, S.M. Multifunctional properties and applications of yttrium ferrite nanoparticles prepared by citrate precursor route. *Mater. Des.* **2017**, *126*, 331–338. [[CrossRef](#)]
38. Ahmad, T.; Phul, R.; Alam, P.; Lone, I.H.; Shahazad, M.; Ahmed, J.; Ahamad, T.; Alshehri, S.M. Dielectric, optical and enhanced photocatalytic properties of CuCrO₂ nanoparticles. *RSC Adv.* **2017**, *7*, 27549–27557. [[CrossRef](#)]
39. Alduhaish, O.; Ubaidullah, M.; Al-Enizi, A.M.; Alhokbany, N.; Alshehri, S.M.; Ahmed, J. Facile Synthesis of Mesoporous α -Fe₂O₃@g-C₃N₄-NCs for Efficient Bifunctional Electrocatalytic Activity (OER/ORR). *Sci. Rep.* **2019**, *9*, 14139. [[CrossRef](#)]
40. Luo, Z.; Martí-Sánchez, S.; Nafria, R.; Joshua, G.; de la Mata, M.; Guardia, P.; Flox, C.; Martínez-Boubeta, C.; Simeonidis, K.; Llorca, J.; et al. Fe₃O₄@NiFe_xO_y Nanoparticles with Enhanced Electrocatalytic Properties for Oxygen Evolution in Carbonate Electrolyte. *ACS Appl. Mater. Interfaces* **2016**, *8*, 29461–29469. [[CrossRef](#)]
41. Zhang, J.; Shang, X.; Ren, H.; Chi, J.; Fu, H.; Dong, B.; Liu, C.; Chai, Y. Modulation of Inverse Spinel Fe₃O₄ by Phosphorus Doping as an Industrially Promising Electrocatalyst for Hydrogen Evolution. *Adv. Mater.* **2019**, *31*, 1905107. [[CrossRef](#)] [[PubMed](#)]
42. Li, S.; Jian, X.; Liu, J.; Guo, S.; Zhou, C.; Zhang, P.; Yang, Y.; Chen, L. Phosphorus-doped Fe₃O₄ nanoflowers grown on 3D porous graphene for robust pH-Universal hydrogen evolution reaction. *Int. J. Hydrog. Energy* **2020**, *45*, 4435–4443. [[CrossRef](#)]
43. Tancredi, P.; Botasini, S.; Moscoso-Londoño, O.; Méndez, E.; Socolovsky, L. Polymer-assisted size control of water-dispersible iron oxide nanoparticles in range between 15 and 100 nm. *Colloids Surf. A Physicochem. Eng. Asp.* **2015**, *464*, 46–51. [[CrossRef](#)]
44. Ahmed, J.; Mao, Y. Delafossite CuAlO₂ Nanoparticles with Electrocatalytic Activity toward Oxygen and Hydrogen Evolution Reactions. In *Nanomaterials for Sustainable Energy*; American Chemical Society: Washington, DC, USA, 2015; Volume 1213, pp. 57–72.
45. Bernal, J.D.; Dasgupta, D.R.; Mackay, A.L. The oxides and hydroxides of iron and their structural inter-relationships. *Clay Miner. Bull.* **2018**, *4*, 15–30. [[CrossRef](#)]
46. Zou, G.; Xiong, K.; Jiang, C.; Li, H.; Li, T.; Du, J.; Qian, Y. Fe₃O₄ Nanocrystals with Novel Fractal. *J. Phys. Chem. B* **2005**, *109*, 18356–18360. [[CrossRef](#)] [[PubMed](#)]
47. Linderoth, S.; Hendriksen, P.V.; Bo/dker, F.; Wells, S.; Davies, K.; Charles, S.W.; Mo/rup, S. On spin-canting in maghemite particles. *J. Appl. Phys.* **1994**, *75*, 6583–6585. [[CrossRef](#)]
48. Brunauer, S.; Deming, L.S.; Deming, W.E.; Teller, E. On a Theory of the van der Waals Adsorption of Gases. *J. Am. Chem. Soc.* **1940**, *62*, 1723–1732. [[CrossRef](#)]
49. Wang, L.; Ji, H.; Wang, S.; Kong, L.; Jiang, X.; Yang, G. Preparation of Fe₃O₄ with high specific surface area and improved capacitance as a supercapacitor. *Nanoscale* **2013**, *5*, 3793–3799. [[CrossRef](#)]
50. Wang, N.; Zhu, L.; Wang, D.; Wang, M.; Lin, Z.; Tang, H. Sono-assisted preparation of highly-efficient peroxidase-like Fe₃O₄ magnetic nanoparticles for catalytic removal of organic pollutants with H₂O₂. *Ultrason. Sonochemistry* **2010**, *17*, 526–533. [[CrossRef](#)]
51. Zhang, X.; Niu, Y.; Meng, X.; Li, Y.; Zhao, J. Structural evolution and characteristics of the phase transformations between α -Fe₂O₃, Fe₃O₄ and γ -Fe₂O₃ nanoparticles under reducing and oxidizing atmospheres. *CrystEngComm* **2013**, *15*, 8166–8172. [[CrossRef](#)]
52. Wang, Y.; Zhang, L.; Gao, X.; Mao, L.; Hu, Y.; Lou, X.W. One-Pot Magnetic Field Induced Formation of Fe₃O₄/C Composite Microrods with Enhanced Lithium Storage Capability. *Small* **2014**, *10*, 2815–2819. [[CrossRef](#)]
53. Li, G.; Li, R.; Zhou, W. A Wire-Shaped Supercapacitor in Micrometer Size Based on Fe₃O₄ Nanosheet Arrays on Fe Wire. *Nano Micro Lett.* **2017**, *9*, 46. [[CrossRef](#)]
54. Alajmi, M.F.; Ahmed, J.; Hussain, A.; Ahamad, T.; Alhokbany, N.; Amir, S.; Ahmad, T.; Alshehri, S.M. Green synthesis of Fe₃O₄ nanoparticles using aqueous extracts of Pandanus odoratissimus leaves for efficient bifunctional electrocatalytic activity. *Appl. Nanosci.* **2018**, *8*, 1427–1435. [[CrossRef](#)]
55. Fujii, T.; de Groot, F.M.F.; Sawatzky, G.A.; Voogt, F.C.; Hibma, T.; Okada, K. In situ XPS analysis of various iron oxide films grown by NO₂-assisted molecular-beam epitaxy. *Phys. Rev. B* **1999**, *59*, 3195–3202. [[CrossRef](#)]
56. Ferraz, L.C.C.; Carvalho, W.M.; Criado, D.; Souza, F.L. Vertically Oriented Iron Oxide Films Produced by Hydrothermal Process: Effect of Thermal Treatment on the Physical Chemical Properties. *ACS Appl. Mater. Interfaces* **2012**, *4*, 5515–5523. [[CrossRef](#)] [[PubMed](#)]

57. Roberts, J.J.P.; Westgard, J.A.; Cooper, L.M.; Murray, R.W. Solution Voltammetry of 4 nm Magnetite Iron Oxide Nanoparticles. *J. Am. Chem. Soc.* **2014**, *136*, 10783–10789. [[CrossRef](#)] [[PubMed](#)]
58. Aljabali, A.A.A.; Barclay, J.E.; Butt, J.N.; Lomonosoff, G.P.; Evans, D.J. Redox-active ferrocene-modified Cowpea mosaic virus nanoparticles. *Dalton Trans.* **2010**, *39*, 7569–7574. [[CrossRef](#)] [[PubMed](#)]
59. Stoerzinger, K.A.; Qiao, L.; Biegalski, M.D.; Shao-Horn, Y. Orientation-Dependent Oxygen Evolution Activities of Rutile IrO₂ and RuO₂. *J. Phys. Chem. Lett.* **2014**, *5*, 1636–1641. [[CrossRef](#)]
60. Ahmed, J.; Trinh, P.; Mugweru, A.M.; Ganguli, A.K. Self-assembly of copper nanoparticles (cubes, rods and spherical nanostructures): Significant role of morphology on hydrogen and oxygen evolution efficiencies. *Solid State Sci.* **2011**, *13*, 855–861. [[CrossRef](#)]
61. Wang, J.; Tang, H.; Ren, H.; Yu, R.; Qi, J.; Mao, D.; Zhao, H.; Wang, D. pH-Regulated Synthesis of Multi-Shelled Manganese Oxide Hollow Microspheres as Supercapacitor Electrodes Using Carbonaceous Microspheres as Templates. *Adv. Sci.* **2014**, *1*, 1400011. [[CrossRef](#)]
62. Du, X.; Wang, C.; Chen, M.; Jiao, Y.; Wang, J. Electrochemical Performances of Nanoparticle Fe₃O₄/Activated Carbon Supercapacitor Using KOH Electrolyte Solution. *J. Phys. Chem. C* **2009**, *113*, 2643–2646. [[CrossRef](#)]
63. Guan, D.; Gao, Z.; Yang, W.; Wang, J.; Yuan, Y.; Wang, B.; Zhang, M.; Liu, L. Hydrothermal synthesis of carbon nanotube/cubic Fe₃O₄ nanocomposite for enhanced performance supercapacitor electrode material. *Mater. Sci. Eng. B* **2013**, *178*, 736–743. [[CrossRef](#)]
64. Zhao, X.; Johnston, C.; Crossley, A.; Grant, P.S. Printable magnetite and pyrrole treated magnetite based electrodes for supercapacitors. *J. Mater. Chem.* **2010**, *20*, 7637–7644. [[CrossRef](#)]
65. Alshehri, S.M.; Ahmed, J.; Alhabarah, A.N.; Ahamad, T.; Ahmad, T. Nitrogen-Doped Cobalt Ferrite/Carbon Nanocomposites for Supercapacitor Applications. *ChemElectroChem* **2017**, *4*, 2952–2958. [[CrossRef](#)]
66. Meng, W.; Chen, W.; Zhao, L.; Huang, Y.; Zhu, M.; Huang, Y.; Fu, Y.; Geng, F.; Yu, J.; Chen, X.; et al. Porous Fe₃O₄/carbon composite electrode material prepared from metal-organic framework template and effect of temperature on its capacitance. *Nano Energy* **2014**, *8*, 133–140. [[CrossRef](#)]



© 2020 by the authors. Licensee MDPI, Basel, Switzerland. This article is an open access article distributed under the terms and conditions of the Creative Commons Attribution (CC BY) license (<http://creativecommons.org/licenses/by/4.0/>).